J. Fluid Mech. (2006), *vol.* 558, *pp.* 253–279. © 2006 Cambridge University Press
doi:10.1017/S0022112006000048 Printed in the United Kingdom

Evolution of toroidal magnetic eddies in an ideal fluid

By Y. HATTORI[1] AND H. K. MOFFATT[2]

[1]Division of Computer Aided Science, Kyushu Institute of Technology, Tobata,
Kitakyushu 804-8550, Japan

[2]Department of Applied Mathematics and Theoretical Physics, University of Cambridge,
Wilberforce Road, Cambridge CB3 0WA, UK

(Received 30 March 2005 and in revised form 12 December 2005)

The magnetohydrodynamic evolution of axisymmetric magnetic eddies within which the magnetic field is purely toroidal with B_θ/r piecewise-constant, and the velocity field is poloidal, is studied both analytically and numerically. A family of exact solutions, generalizing Hill's spherical vortex to the case of non-zero magnetic field, is found. These exact solutions are (like Hill's vortex) unstable, so that, under weak disturbance, a narrow spike of vorticity is shed from the neighbourhood of the rear stagnation point. Numerical simulation using a contour-dynamics formulation shows that, for general initial contour shape, a contour singularity appears at a finite time t^*, like that which appears on a disturbed vortex sheet. Techniques of regularization and sample-point redistribution are used so that the eddy contours can be tracked well beyond t^*. When the fluid is initially at rest, the magnetic eddy first contracts towards the axis of symmetry under the action of its Lorentz force distribution; then two spherical fronts form, which propagate in the two opposite directions along the axis of symmetry, in a manner captured well by the exact solution. The magnetic energy remains bounded away from zero despite the fact that there is no topological barrier to its further decrease. Magnetic eddy evolution and the possible existence of steady states under a uniform compressive strain field is also numerically investigated.

1. Introduction

A problem of fundamental interest in magnetohydrodynamics (MHD) has been posed by Moffatt (1985): suppose that at some initial instant, a magnetic field $\boldsymbol{B}_0(\boldsymbol{x})$ of bounded support exists in a perfectly conducting fluid at rest. For $t > 0$, the fluid moves under the action of the Lorentz force associated with the field distribution, and carries the field with it. If the fluid is viscous, then energy is dissipated for as long as the fluid moves, and so the field seeks a magnetostatic configuration of minimal magnetic energy compatible with its prescribed (and invariant) topology. The problem is to determine the asymptotic field, given simply the initial field distribution. An important invariant of the field is its magnetic helicity

$$H_M = \int \boldsymbol{A} \cdot \boldsymbol{B} \, \mathrm{d}V, \tag{1.1}$$

a quantity that provides a measure of the topological complexity (as characterized by linkage of field lines) of the field (Moffatt 1969). When H_M is non-zero, this invariant provides a topological barrier to the decrease of magnetic energy, which is bounded below by a constant proportional to $|H_M|$ (Arnold 1974; Moffatt 1985).

Various variants of this problem can be posed; first, we may consider what happens if the fluid is inviscid as well as perfectly conducting. In this situation, we have two further invariants during the magnetohydrodynamic evolution,

the total energy:

$$E_T = E_H + E_M = \frac{1}{2}\int (u^2 + B^2)\,\mathrm{d}V, \tag{1.2}$$

and the cross-helicity:

$$H_C = \int \boldsymbol{u}\cdot\boldsymbol{B}\,\mathrm{d}V. \tag{1.3}$$

If the fluid is initially at rest or in purely irrotational motion, then the cross-helicity is zero, and remains zero for all time. The magnetic energy will still decrease, at least initially, but now with a compensating increase of kinetic energy. If H_M is non-zero then the same lower bound as before persists for the magnetic energy, but there is now no guarantee that the field will settle down to a steady state; it may well oscillate for all time around some equilibrium configuration.

The situation is very different if there is no linkage in the initial field configuration (so that $H_M = 0$). There is then no topological barrier to sustained decrease of magnetic energy, and it is conceivable that this may fall to zero, all the magnetic energy being simply converted to kinetic energy. In this paper, we examine the simplest situation of this type, for which the initial field has the form $\boldsymbol{B}_0 = (0, B(r, z), 0)$ in cylindrical polar coordinates (r, θ, z), so that the $\boldsymbol{B}$-lines are circular and unlinked. The Lorentz force associated with Maxwell tension in the field lines tends to make these contract towards the axis of symmetry; however, we shall find that an initial magnetic 'blob' does not contract indefinitely towards the axis, but only to a distance determined by the initial conditions; it then separates into two 'magnetic eddies' with nearly spherical 'fronts', which propagate in the two opposite directions along the axis of symmetry.

A variant of this problem is to suppose that the magnetic blob is subjected to a compressive uniform strain of the form $\boldsymbol{U} = (Sr, 0, -2Sz)$ with $S > 0$. This obviously tends to flatten any magnetic blob of compact support to a disk-shape near the plane $z = 0$, and the question naturally arises as to whether there are any equilibrium states in which the contracting tendency of the Lorentz force is balanced by this flattening tendency of the strain field. This problem was originally discussed for a viscous fluid by Moffatt (1963); the motivation came from the MHD of the turbulent interstellar medium where kinematic viscosity ν is much greater than magnetic diffusivity η; on the sub-Kolmogorov scale, the velocity gradient is approximately uniform, but the magnetic field is still nearly 'frozen-in'; the relevance of the above problem is then clear. Recent work of Schekochihin *et al.* (2001) has focused renewed attention on this type of situation. In § 6, we shall reconsider the problem posed by Moffatt (1963), but again limiting attention to the case of an inviscid fluid.

The contour-dynamics formulation developed in this paper has potentially important application to the more general problem, important in astrophysics, of understanding the behaviour of isolated magnetic flux tubes, and the manner in which these can interact and reconnect. Previous studies have either adopted a thin-tube approximation (see, for example, Spruit 1981; Ferriz-Mas & Schüssler 1993) which takes no account of deformation of the tube cross-section, or have used direct numerical simulation at much lower values of the magnetic Reynolds number than are relevant for astrophysical applications. We shall show in this paper that contour dynamics offers a promising alternative approach to problems of this kind.

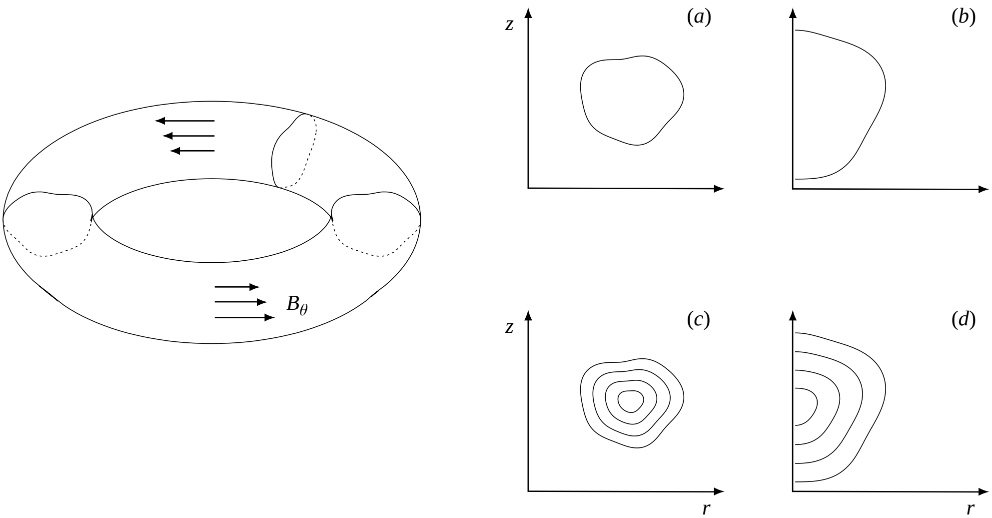

FIGURE 1. Magnetic eddy and cross-sections: (a, c) toroidal topology; (b, d) spherical topology.

2. Contour-dynamics formulation

2.1. *Statement of the problem*

We consider an axisymmetric MHD flow whose velocity and magnetic fields are respectively poloidal and toroidal: $\boldsymbol{u} = (u_r(r, z, t), 0, u_z(r, z, t))$, $\boldsymbol{B} = (0, B_\theta(r, z, t), 0)$, where (r, θ, z) is a cylindrical coordinate system (figure 1). The fluid is treated as ideal and magnetic diffusivity and kinematic viscosity are set to zero. We assume that the magnetic field is confined to a compact patch D in the (r, z)-plane and is proportional to r inside the patch: $B_\theta = \kappa r$; this is the only toroidal field distribution that remains invariant under the convective and stretching action of an axisymmetric poloidal flow. The corresponding current is uniform inside the patch, the current lines closing in a surface current on the patch boundary. The blob obtained by rotating D about the z-axis is either topologically toroidal (figure 1*a*) or topologically spherical (figure 1*b*). We shall also consider the more general situation in which the patch is divided into regions in which κ takes different values: $B_\theta = \kappa_i r$ (figure 1*c*,*d*).

2.2. *Contour-dynamics formulation*

The governing magnetohydrodynamic equations for an incompressible ideal fluid are

$$\rho \frac{\mathrm{D}\boldsymbol{u}}{\mathrm{D}t} = -\nabla p + \boldsymbol{J} \times \boldsymbol{B}, \tag{2.1}$$

$$\frac{\partial \boldsymbol{B}}{\partial t} = \nabla \times (\boldsymbol{u} \times \boldsymbol{B}), \tag{2.2}$$

$$\nabla \cdot \boldsymbol{u} = \nabla \cdot \boldsymbol{B} = 0, \quad \mu \boldsymbol{J} = \nabla \times \boldsymbol{B}, \tag{2.3}$$

where ρ and μ are the (constant) density and permeability, and $\mathrm{D}/\mathrm{D}t = \partial_t + u_r \partial_r + u_z \partial_z$. We let $\tilde{p} = p/\rho$ and $\tilde{\boldsymbol{B}} = \boldsymbol{B}/\sqrt{\mu\rho}$ and drop the tilde in the following. Since for a purely toroidal field, the Lorentz force $\boldsymbol{J} \times \boldsymbol{B}$ reduces to $\nabla(B_\theta^2/2) - B_\theta^2/r$, the equations of motion reduce to

$$\frac{\mathrm{D}u_r}{\mathrm{D}t} = -\frac{\partial p_*}{\partial r} - \kappa^2 r H[f(r, z, t)], \tag{2.4}$$

$$\frac{Du_z}{Dt} = -\frac{\partial p_*}{\partial z}, \tag{2.5}$$

$$\frac{Df}{Dt} = 0, \tag{2.6}$$

$$\frac{\partial u_r}{\partial r} + \frac{u_r}{r} + \frac{\partial u_z}{\partial z} = 0. \tag{2.7}$$

Here, $p_* = p + (B_\theta^2/2)$, and $f(r, z, t) = 0$ describes the patch boundary with $f > 0$ on the inside; $H(\cdot)$ is the Heaviside function. Note that the induction equation

$$\frac{D}{Dt}\left(\frac{B_\theta}{r}\right) = 0 \tag{2.8}$$

is satisfied by the choice $B_\theta = \kappa r H\,[f(r, z, t)]$ and (2.6).

Using the Stokes streamfunction $\Psi(r, z)$, the velocity components are

$$u_r = -\frac{1}{r}\frac{\partial \Psi}{\partial z}, \quad u_z = \frac{1}{r}\frac{\partial \Psi}{\partial r}, \tag{2.9}$$

and the vorticity (in the θ-direction) is

$$\omega = -\frac{1}{r}D^2\Psi, \tag{2.10}$$

where

$$D^2 = \frac{\partial^2}{\partial r^2} - \frac{1}{r}\frac{\partial}{\partial r} + \frac{\partial^2}{\partial z^2}. \tag{2.11}$$

Equation (2.10) may be inverted to give

$$\Psi(r, z) = \iint \omega(r', z')G(r, z|r', z')\,dr'dz', \tag{2.12}$$

$$G(r, z|r', z') = \frac{1}{2\pi}(rr')^{1/2}\left[\left(\frac{2}{k} - k\right)K(k) - \frac{2}{k}E(k)\right], \tag{2.13}$$

$$k^2 = \frac{4rr'}{(r + r')^2 + (z - z')^2}, \tag{2.14}$$

where $K(k)$ and $E(k)$ are the complete elliptic integrals of the first and second kinds.

The vorticity equation reads

$$\frac{D}{Dt}\left(\frac{\omega}{r}\right) = -\kappa^2\frac{\partial f}{\partial z}\delta[f(r, z, t)]. \tag{2.15}$$

Note that the Lorentz force is irrotational except at the patch boundary, and (2.15) tells us that ω/r is conserved on a particle path except on this boundary where surface vorticity is generated. We assume that the vorticity is initially zero everywhere except possibly on the patch boundary; the vorticity then remains zero everywhere except on the patch boundary, where a non-uniform vortex sheet develops in time. Thus we may write

$$\omega/r = \Omega(r, z, t)\delta\,[f(r, z, t)]\,|\nabla f|, \tag{2.16}$$

where Ω is the local strength of the sheet. Substituting in (2.15) and using (2.6), we obtain

$$\frac{D\Omega}{Dt} = -\kappa^2\frac{1}{|\nabla f|}\frac{\partial f}{\partial z} - \Omega\frac{1}{|\nabla f|}\frac{D|\nabla f|}{Dt}. \tag{2.17}$$

Now, let s be a parameter taken clockwise along the patch boundary in the (r, z)-plane, and let $(r, z) = (R(s, t), Z(s, t))$ be the corresponding parametric representation of this boundary. Then

$$\frac{\partial R}{\partial t} = u_r(R, Z, t), \quad \frac{\partial Z}{\partial t} = u_z(R, Z, t), \tag{2.18}$$

and it follows from (2.6) that

$$\frac{1}{|\nabla f|}\frac{\mathrm{D}|\nabla f|}{\mathrm{D}t} = -\boldsymbol{n}\cdot[(\boldsymbol{n}\cdot\nabla)\boldsymbol{u}] = \frac{1}{L}\frac{\partial L}{\partial t} + \frac{u_r}{r}, \quad \boldsymbol{n} = \frac{\nabla f}{|\nabla f|}, \tag{2.19}$$

where

$$L^2(s, t) \equiv \left(\frac{\partial R}{\partial s}\right)^2 + \left(\frac{\partial Z}{\partial s}\right)^2.$$

The streamfunction is now

$$\begin{aligned}\Psi(r, z) &= \iint r' G(r, z|r', z')\Omega(r', z', t)\delta\left[f(r', z', t)\right]|\nabla f|\,\mathrm{d}r'\,\mathrm{d}z' \\ &= \oint \Omega(s, t)R(s, t)G(r, z|R(s, t), Z(s, t))L(s, t)\,\mathrm{d}s,\end{aligned} \tag{2.20}$$

where $\oint$ denotes an integral along the patch boundary and Ω is now a function of s and t. We take the principal value at $(r, z) = (R(s, t), Z(s, t))$ where the integrand is singular. Equation (2.17) may now be written

$$\frac{\partial \Omega}{\partial t} = \kappa^2 \cos\Theta(s, t) - \Omega\left(\frac{1}{L}\frac{\partial L}{\partial t} + \frac{1}{R}\frac{\partial R}{\partial t}\right), \tag{2.21}$$

where $\Theta(s, t)$ is the angle between the r-axis and the boundary, i.e.

$$\cos\Theta = \frac{1}{L}\frac{\partial R}{\partial s}. \tag{2.22}$$

If we introduce $\gamma = \Omega L R$, equation (2.21) is simplified since

$$\frac{\partial \gamma}{\partial t} = \frac{\partial \Omega}{\partial t}LR + \Omega\frac{\partial L}{\partial t}R + \Omega L\frac{\partial R}{\partial t}.$$

In fact γ corresponds to the Lagrangian parameter for a vortex sheet without magnetic fields; $\mathrm{d}\gamma$ is the circulation in the small area which includes a portion $\mathrm{d}s$ of the patch boundary. To summarize, the equations of motion are

$$\frac{\partial \gamma}{\partial t} = \kappa^2 R\frac{\partial R}{\partial s}, \tag{2.23}$$

$$\frac{\partial R}{\partial t} = u_r(R(s, t), Z(s, t), t), \quad \frac{\partial Z}{\partial t} = u_z(R(s, t), Z(s, t), t), \tag{2.24}$$

$$u_r(r, z) = -\frac{1}{r}\oint \gamma(s, t)\left[\frac{\partial}{\partial z}G(r, z|R(s, t), Z(s, t))\right]\mathrm{d}s, \tag{2.25}$$

$$u_z(r, z) = \frac{1}{r}\oint \gamma(s, t)\left[\frac{\partial}{\partial r}G(r, z|R(s, t), Z(s, t))\right]\mathrm{d}s. \tag{2.26}$$

These five equations form a closed set of equations on the boundary.

The above formulation for a patch, or single contour, can be readily extended to multiple contours. For, consider a magnetic field of the form

$$\frac{B_\theta}{r} = \sum_{i=1}^{m} \Delta\kappa_i H[f_i(r, z, t)], \tag{2.27}$$

$$\Delta\kappa_i = \kappa_i - \kappa_{i-1} > 0, \quad \kappa_0 = 0, \tag{2.28}$$

where $f_i = 0$ corresponds to the ith contour, which separates the regions in which $B_\theta/r = \kappa_{i-1}$ and κ_i. We assume that the contours do not intersect, so that

$$f_i(r, z, t) > f_j(r, z, t) \ \text{ for } i < j. \tag{2.29}$$

Then the equations of motion are

$$\frac{\partial \gamma_i}{\partial t} = A_i R_i \frac{\partial R_i}{\partial s_i}, \tag{2.30}$$

$$\frac{\partial R_i}{\partial t} = u_r(R_i(s_i, t), Z_i(s_i, t), t), \qquad \frac{\partial Z_i}{\partial t} = u_z(R_i(s_i, t), Z_i(s_i, t), t), \tag{2.31}$$

$$u_r(r, z) = -\frac{1}{r}\sum_{i=1}^{m} \oint_i \gamma_i(s_i, t)\left[\frac{\partial}{\partial z} G(r, z|R_i(s_i, t), Z_i(s_i, t))\right] \mathrm{d}s_i, \tag{2.32}$$

$$u_z(r, z) = \frac{1}{r}\sum_{i=1}^{m} \oint_i \gamma_i(s_i, t)\left[\frac{\partial}{\partial r} G(r, z|R_i(s_i, t), Z_i(s_i, t))\right] \mathrm{d}s_i, \tag{2.33}$$

where

$$A_i = (\Delta\kappa_i)^2 + 2\sum_{j=1}^{i-1} \Delta\kappa_i \Delta\kappa_j = \kappa_i^2 - \kappa_{i-1}^2. \tag{2.34}$$

2.3. *Conservation laws*

The total energy E_T and the volume fractions V_i of the eddy are conserved. The total energy is

$$E_T = E_H + E_M, \tag{2.35}$$

where the hydrodynamic energy E_H and the magnetic energy E_M are now given by

$$E_H = \frac{1}{2}\int u^2 = \pi \sum_i \oint_i \gamma_i(s_i, t)\Psi(R_i(s_i, t), Z_i(s_i, t), t)\,\mathrm{d}s_i, \tag{2.36}$$

$$E_M = \frac{1}{2}\int B^2 = \frac{\pi}{4}\sum_i A_i \oint_i r^4 n_r\,\mathrm{d}l_i, \tag{2.37}$$

Here $\mathrm{d}l_i = L_i \mathrm{d}s_i$ and $\boldsymbol{n} = (n_r, n_z)$ denotes the outward unit normal to the contours. The volume inside the ith contour is

$$V_i = \int_{T_i} \mathrm{d}V = \pi \oint_i r^2 n_r\,\mathrm{d}l_i. \tag{2.38}$$

2.4. *Relation with other problems*

The equations derived above are related to those that have been previously obtained for the nonlinear evolution of Kelvin–Helmholtz (vortex sheet) and Rayleigh–Taylor instability. In fact, if we replace the right hand-side of (2.23) by zero, so that the strength of the sheet is constant (at constant s), the present equations become equivalent to those derived by Caflisch, Li & Shelley (1993) for the evolution of an axisymmetric vortex sheet. On the other hand, the boundary-integral formulation of the Rayleigh–Taylor instability deals with a vortex sheet whose strength varies in time (Baker, Meiron & Orszag 1980, 1982). There are two differences from the present case. First, in the Rayleigh–Taylor instability, the driving force is constant in regions separated by the vortex sheet, whereas in the present case the driving force, $\kappa_i^2 r$ in the ith region, depends on position. Second, the rate of change of sheet strength has several terms essentially due to discontinuity in density in the Rayleigh–Taylor instability; equation (2.23) is rather simple in the present case since the density is constant everywhere.

3. A family of exact solutions

We show in this section that there exists a family of exact solutions to (2.23)–(2.26) representing magnetic vortices of spherical structure that translate without change of shape. These are related to Hill's spherical vortex for the classical hydrodynamic situation, and indeed include Hill's vortex as a limiting case.

The magnetic vortex is steady in a moving frame $(r, z_*) = (r, z - U_0 t)$, and is given by

$$\Psi(r, z_*) = \begin{cases} \frac{3}{4} U_0' r^2 [1 - (\sigma/R_0)^2], & \sigma < R_0, \\ -\frac{1}{2} U_0 r^2 [1 - (R_0/\sigma)^3], & \sigma > R_0, \end{cases} \tag{3.1}$$

where $\sigma^2 = r^2 + {z_*}^2$, and

$$f(r, z_*) = \begin{cases} \Psi/U_0', & \sigma < R_0, \\ \Psi/U_0, & \sigma > R_0, \end{cases} \qquad \Omega(r, z_*) = \frac{3}{2R_0}(U_0 - U_0'). \tag{3.2}$$

The total pressure is obtained from equations (2.4) and (2.5) in the form

$$p_* = \begin{cases} p_0 - \frac{1}{2}\kappa^2 r^2 - \frac{1}{2}u^2 - \dfrac{15U_0'}{2R_0^2}\Psi, & \sigma < R_0, \\ p_\infty + \frac{1}{2}U_0^2 - \frac{1}{2}u^2, & \sigma > R_0. \end{cases} \tag{3.3}$$

Since $u = 3U_0 r/2R_0$ at $\sigma = R_{0+}$ and $u = 3U_0' r/2R_0$ at $\sigma = R_{0-}$, continuity of this total pressure across the boundary $\sigma = R_0$ requires that

$$U_0^2 - {U_0'}^2 = \left(\tfrac{2}{3}\kappa R_0\right)^2 . \tag{3.4}$$

The velocity field given by (3.1) is that of the classical Hill's vortex but with different velocities U_0 outside the sphere $\sigma = R_0$ and U_0' inside, this difference being accommodated by a vortex sheet of appropriate strength on $\sigma = R_0$. In particular, the case $U_0 = U_0'$, which implies $\kappa = 0$, corresponds to Hill's spherical vortex. For $U_0 = -U_0'$, which also implies $\kappa = 0$, the velocity field inside the sphere is that of Hill's vortex with the opposite sign; in this case, the vortex sheet on the boundary, whose strength is $\Omega = -3U_0/R_0$, keeps the solution steady without a magnetic field. For $|U_0| \neq |U_0'|$, the magnetic field together with the vortex sheet on the surface of the sphere makes the inside translate with the velocity U_0.

The contour-dynamics equations obtained above show that the increase of γ through (2.23) is balanced by convection and stretching along the boundary. Thus, if we take $s = \varphi$ at $t = t_0$ with φ taken clockwise from the z-axis, γ increases by

$$\kappa^2 R_0^2 \cos\varphi \sin\varphi \Delta t, \tag{3.5}$$

in the time interval $[t_0, t_0+\Delta t]$. Since the segment $\varphi_0 < \varphi < \varphi_0 + \Delta\varphi$ is convected to

$$\varphi_0 + \left.\frac{u_\varphi}{R_0}\right|_{\varphi_0} \Delta t < \varphi < \varphi_0 + \Delta\varphi + \left(\left.\frac{u_\varphi}{R_0}\right|_{\varphi_0} + \frac{1}{R_0}\left.\frac{\partial u_\varphi}{\partial\varphi}\right|_{\varphi_0} \Delta\varphi \right) \Delta t, \tag{3.6}$$

where u_φ is the velocity along the boundary, γ should be divided by

$$1 + \frac{1}{R_0}\left.\frac{\partial u_\varphi}{\partial\varphi}\right|_{\varphi_0} \Delta t, \tag{3.7}$$

if we relabel the particles as $s=\varphi$ at $t=t_0+\Delta t$. The result should coincide with γ at

$$s = \varphi_0 + \left.\frac{u_\varphi}{R_0}\right|_{\varphi_0} \Delta t. \tag{3.8}$$

This requirement gives

$$\kappa^2 R_0^2 \sin\varphi\cos\varphi - \gamma \left.\frac{1}{R_0}\frac{\partial u_\varphi}{\partial\varphi}\right|_{\varphi_0} = \left.\frac{1}{R_0}\frac{\partial\gamma}{\partial\varphi}\right|_{\varphi_0} u_\varphi. \tag{3.9}$$

It is easy to check that this relation is satisfied by virtue of (3.4) and the relations

$$u_\varphi = \tfrac{1}{2}(u_\varphi|_{\sigma=R_{0+}} + u_\varphi|_{\sigma=R_{0-}}), \quad \gamma = R_0^2(u_\varphi|_{\sigma=R_{0+}} - u_\varphi|_{\sigma=R_{0-}}). \tag{3.10}$$

The solutions above have finite energy in the frame in which the fluid is at rest at infinity:

$$E_H = \pi R_0^3\left(U_0^2 + \frac{3}{7}U_0'^2\right) = \pi R_0^3 U_0^2\left(\frac{10}{7} - \frac{4\kappa^2R_0^2}{21U_0^2}\right), \tag{3.11}$$

$$E_M = \frac{3}{5}\pi R_0^3\left(U_0^2 - U_0'^2\right) = \frac{4}{15}\pi\kappa^2R_0^5, \tag{3.12}$$

$$E_T = \pi R_0^3\left(\frac{8}{5}U_0^2 - \frac{6}{35}U_0'^2\right) = \pi R_0^3 U_0^2\left(\frac{10}{7} + \frac{8\kappa^2R_0^2}{105U_0^2}\right). \tag{3.13}$$

In particular, for $U_0'=0$,

$$E_H = \pi R_0^3 U_0^2, \quad E_M = \tfrac{3}{5}\pi R_0^3 U_0^2, \quad E_T = \tfrac{8}{5}\pi R_0^3 U_0^2, \tag{3.14}$$

giving the energy ratio $E_M/E_H = 3/5$.

4. Numerical procedure

We now describe some numerical simulations of equations (2.23)–(2.26) or (2.30)–(2.33). Each contour is represented by a finite number of points: $s_{i,j} = j/N_i$, $j = 1, \ldots, N_i$. The line integrals in (2.25) and (2.26) or (2.32) and (2.33) are evaluated by the trapezoidal formula. The integrands diverge at $(r,z)=(r',z')$; but following Pozrikidis (1986), we subtract the asymptotic forms of the integrands for which the principal values can be evaluated analytically on the arc connecting $(r,z)=(r',z')$ and its neighbouring points from the singular integrands. The remainders, which do not diverge, are integrated numerically. Equations (2.23) and (2.24), or (2.30) and (2.31), are advanced by the fourth-order Runge–Kutta method.

Except in § 4.3, where the exact solution is numerically checked, the strength of the vortex sheet is assumed to be zero at $t=0$; in other words, the fluid is initially at rest for the cases without imposed strain.

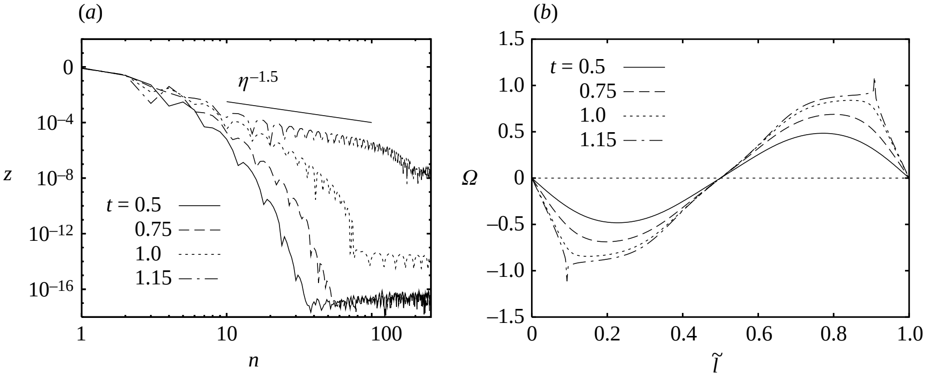

FIGURE 2. Appearance of singularity. (*a*) Log-linear plot of the Fourier amplitudes. (*b*) Strength of vortex sheet as a function of normalized length.

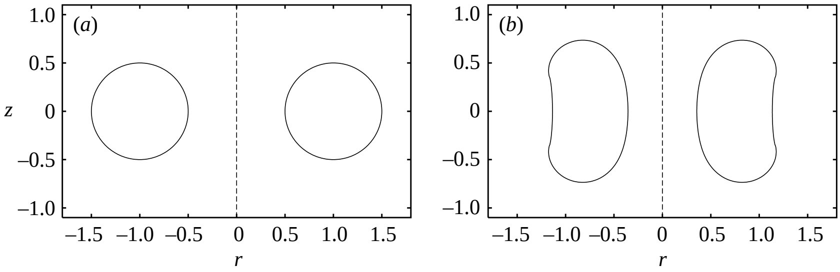

FIGURE 3. Evolution of the magnetic torus. (*a*) $t = 0$, (*b*) $t = 1.15$ (around the appearance of singularity).

There are two techniques that need a word of explanation: regularization and redistribution of points. We describe these techniques using, by way of example, the case of a torus with circular core $r_c/R_0 = 0.5$. The variables are non-dimensionalized by the time scale κ^{-1}, and the length scale R_0 (the initial larger radius of the torus).

4.1. *Singularities and regularization*

It is well-known that singularities can develop on a vortex sheet in a finite time (Moore 1979; Krasny 1986; Caflisch *et al.* 1993; Sakajo 2002). Here, we encounter the same type of singularity on a contour. Figure 2 shows the evolution of the spectrum and sheet-strength distribution. We have applied a Fourier filter (Krasny 1986) to suppress numerical irregularities. At $t \approx 1.15$, the spectrum decays algebraically as $n^{-1.5}$, and the sheet strength has cusps at the symmetrically placed points $\tilde{l} \approx 0.09$ and 0.91. As Krasny (1986) has shown, these features are clear signs of singularities. The magnetic torus contracts towards the z-axis as a result of the inward Lorentz force $\kappa^2 r$ (figure 3). The singularities, however, emerge so quickly that we cannot follow the evolution of the contour for very long.

We regularize these singularities by introducing a finite-core-size effect as adopted by Krasny (1987) and Caflisch *et al.* (1993). This is achieved by modifying the Biot-Savart law as follows:

$$\boldsymbol{A} = \frac{1}{4\pi}\int \frac{\boldsymbol{\omega}}{r}\,\mathrm{d}\boldsymbol{x}' \rightarrow \frac{1}{4\pi}\int \frac{\boldsymbol{\omega}}{(r^2+\epsilon^2)^{1/2}}\,\mathrm{d}\boldsymbol{x}'. \tag{4.1}$$

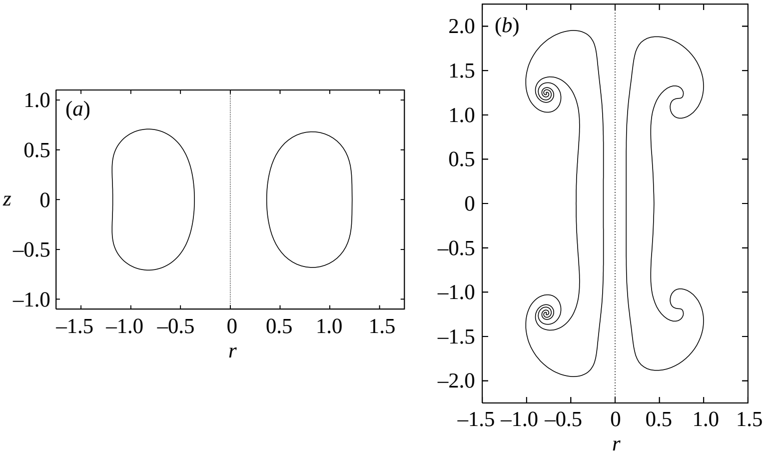

FIGURE 4. Regularized simulation. Cross-sections: (left) $\epsilon = 0.05$, (right) $\epsilon = 0.1$. (*a*) $t = 1.15$, (*b*) $t = 3.5$.

The regularized Green function is formally the same as the original, except for a modification in k:

$$G(r, z|r', z') = \frac{1}{2\pi}(rr')^{1/2}\left[\left(\frac{2}{k} - k\right)K(k) - \frac{2}{k}E(k)\right], \tag{4.2}$$

where now

$$k^2 = \frac{4rr'}{(r + r')^2 + (z - z')^2 + \epsilon^2}. \tag{4.3}$$

Note that this regularization does not affect the conservation laws; both the total energy and the volume are invariants of the motion with the regularized Green function. Figure 4 shows results with this regularized Green function, with regularization parameter ϵ set to 0.05 and 0.1. The cross-section at $t = 1.15$ (figure 4*a*) is quite similar to that for $\epsilon = 0$ (figure 3*b*). We can continue the simulation for a much longer time with $\epsilon = 0.05$ and 0.1. At $t = 3.5$, the torus has contracted further towards the z-axis and is stretched in the z-direction. The contour rolls up at $(r, z) \approx (0.8, \pm 1.25)$. Both the total energy and the volume are conserved within errors less than 0.04 % for $0 \leqslant t \leqslant 2.5$.

The regularized Green function is used in all the numerical results that follow. The fine-scale structures do depend on the value of ϵ, but the global motion is fairly insensitive to ϵ, provided it is small (see figure 4). For the roll-up region we may expect scaling laws as in Nitsche, Taylor & Krasny (2003). (It is also known that for the case of a vortex sheet (Tryggvason, Dahm & Sbeih 1991; Nitsche *et al.* 2003) the global motion with the regularized Green function converges as the regularization parameter decreases to the same limit as the small-viscosity limit in a Navier–Stokes simulation.)

4.2. *Redistribution of points*

As time proceeds in the numerical simulation, the points which represent the contour can become too sparse or too dense, depending on their positions, to keep sufficient precision; for example, the error in volume conservation grows to 0.8 % at $t = 3.5$. To overcome this problem, we redistribute points every 20–40 steps. There are two criteria for redistribution: the maximum distance $\Delta l_{\max}$ between the points and the

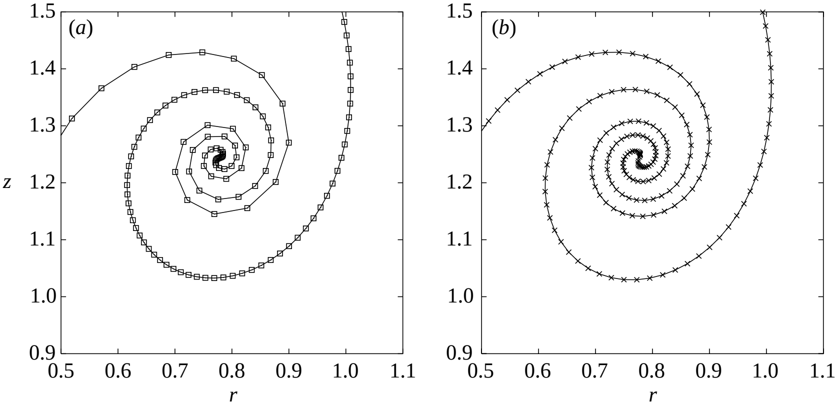

FIGURE 5. Effect of redistribution. Magnified view of spirals. $t = 3.5$. (*a*) Without redistribution, (*b*) with redistribution.

maximum angle $\Delta\phi_{\max}$ between adjacent arcs. In other words, a new point is created whenever necessary to ensure that the distance and the angle do not exceed $\Delta l_{\max}$ and $\Delta\phi_{\max}$, respectively. In practice, we connect the old points by cubic spline and distribute new points consecutively with the distance

$$\Delta l = \Delta l_{\max} \tanh\left(\frac{R_* \Delta\phi_{\max}}{\Delta l_{\max}}\right),$$

where R_* is the radius of curvature of the arc. Note that Δl is a smooth function of R_* satisfying

$$\begin{aligned} \Delta l &\to \Delta l_{\max} \quad \text{as } R_* \to \infty, \\ \Delta l &\to R_* \Delta\phi_{\max} \quad \text{as } R_* \to 0. \end{aligned}$$

In the following calculations, $\Delta\phi_{\max}$ and $\Delta l_{\max}$ are set to 0.08π and 0.5ϵ. The results are almost unchanged by using lower values of $\Delta\phi_{\max}$ and $\Delta l_{\max}$. The new points are parametrized with a constant increment. The sheet strength should be unchanged by change of parameterization $s \to s'$, implying $\gamma(s)/L(s) = \gamma'(s')/L'(s')$.

The redistribution keeps the magnetic energy and the volume almost unchanged, but it produces a certain amount of error in the hydrodynamic energy; this is probably due to small but non-negligible errors in interpolation and numerical differentiation. This error is eliminated by scaling γ, i.e. by multiplying γ by a factor close to unity so that the new hydrodynamic energy is equal to the old value. This rescaling does not change the magnetic energy or the volume since these are independent of γ.

Figure 5 compares cases without and with redistribution. The number of points increases monotonically in most cases from $N = 100$–200 initially to $N = 1000$–2000 at the end of the calculation.

4.3. *Numerical test of exact solution*

It is of interest to check numerically the exact solution found in § 3. Figure 6 compares the cross-sections of the numerical solution (solid line) and the exact solution (dashed line). We set $U_0' = 0$; the flow inside the sphere is uniform. The regularization parameter ϵ is set to 0.05. The agreement is reasonable except around the rear where an instability appears. This instability is similar to that of Hill's vortex, as described by Moffatt & Moore (1978) and numerically confirmed by Pozrikidis

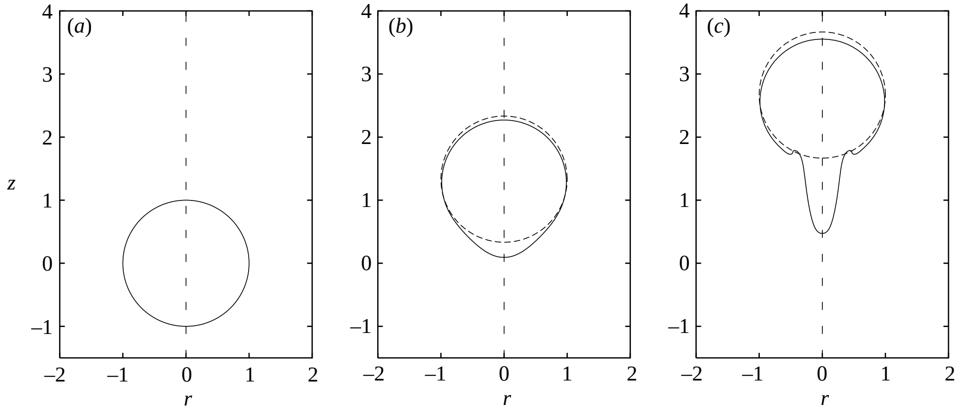

FIGURE 6. Numerical test of exact solution. Cross-section. Solid lines: simulation, dashed lines: exact solution. (a) $t = 0$, (b) $t = 2$, (c) $t = 4$. The 'spike' instability near the rear stagnation point is evident.

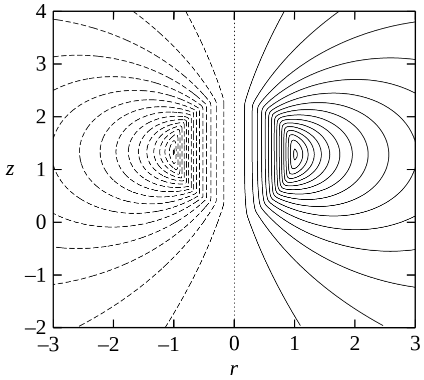

FIGURE 7. Numerical test of exact solution. Streamlines at $t = 2$: solid lines (right), simulation; dashed lines (left), exact solution.

(1986); it arises from the sweeping of any perturbation of the spherical boundary round towards the rear stagnation point where the perturbation accumulates. The speed of the sphere is estimated as 0.64 using the position of the front, which is close to the exact value 2/3 in the present non-dimensionalization.

Figure 7 compares the streamlines of the numerical solution (right, solid lines) and the exact solution (left, dashed lines) at $t = 2$. The agreement is good. Inside the sphere centred at $(r, z) \approx (0, 1.2)$ the flow is almost uniform; outside the sphere the exact streamlines are those of Hill's vortex.

5. Motion without strain

5.1. *Simulation parameters*

We consider eddies of either toroidal or spherical topology (figure 1). The initial shapes of contours are listed for the cases without strain in tables 1 and 2.

In table 1, a_c and b_c are the lengths of the r- and z-axes of the core for the torus cases and in table 2, a, b are the same measures of the section for the sphere cases. For the torus case, the circular core with $r_c = 0.5$ is studied as a basic prototype. The

Case	Topology	Core/Cross-section	Parameters
TC	Torus	Circular	$r_c = 0.1, 0.3, \underline{0.5}, 0.8$
TE	Torus	Elliptic	$(a_c, b_c) = (0.9, 0.2778), (0.25, 1)$
SC	Sphere	Circular	$(a, b) = \underline{(1, 1)}$
SE	Sphere	Elliptic	$(a, b) = (0.5, 2), (2, 0.5)$

TABLE 1. The initial shapes of contours for single-contour cases ($m = 1$). Underlined values denote the basic prototype.

Case	Topology	Core/Cross-section	Parameters
TC	Torus	Circular	$r_c = 0.5$
SC	Sphere	Circular	$(a, b) = (1, 1)$

TABLE 2. The initial shapes of contours for multiple-contour cases ($m = 1, 2, 4, 8$).

two cases with elliptic core are chosen so that this core has the same area as for the basic case and does not touch the z-axis. For the spherical topology cases, the case of a true sphere $(a, b) = (1, 1)$ is studied as a basic prototype.

The regularization parameter ϵ is set to $0.1 r_c$ for the torus cases with circular cores and 0.05 otherwise. Since all the cases considered in the following have symmetry with respect to the plane $z = 0$, only the region $r, z \geqslant 0$ is shown in the figures of cross-section.

5.2. *Single contour: $m = 1$*

5.2.1. *Evolution of the contour*

Figure 8 shows the time evolution of the cross-section of the eddy, or the contour, for the torus case with a circular core $r_c = 0.5$. Starting from figure 8(a), the torus contracts towards the z-axis and is stretched in the z-direction (figure 8b, c). Roll-up starts around $t = 2$ (figure 8c) and then spirals are formed (figure 8d). The number of turns of the spirals increases in time. On the other hand, the region above/below the upper/lower spiral forms a spherical front with a hole around the z-axis, which moves steadily along the z-axis. The region between the two spirals becomes thin as the fronts move outward, while the speed of contraction becomes small in the later stage. At $t = 5.5$ (figure 8g), an instability is observed around the outer end of the spiral and structures which are much smaller than the regularization parameter ϵ start to develop. Since these fine-scale structures induce irregular motions which are not observed for Navier–Stokes solutions (Nitsche *et al.* 2003), we stop the calculation when they become so large that the global motion is affected in an unphysical way.

Figure 9 shows the time evolution of the contour for the sphere case $(a, b) = (1, 1)$. First the contour contracts towards the z-axis. The top and bottom parts form spherical fronts whose radii are nearly unchanged after $t = 2$; they move steadily outwards. The body part between the spherical fronts is parallel to the z-axis for $|z| \leqslant 1.2$–1.5 for $t \geqslant 4$. The motion within this body is very slow, tending to a ‘magnetic cylinder’ for which

$$u_r = u_z = 0, \quad B_\theta = \begin{cases} \kappa r, & r < R_0, \\ 0, & r > R_0. \end{cases} \tag{5.1}$$

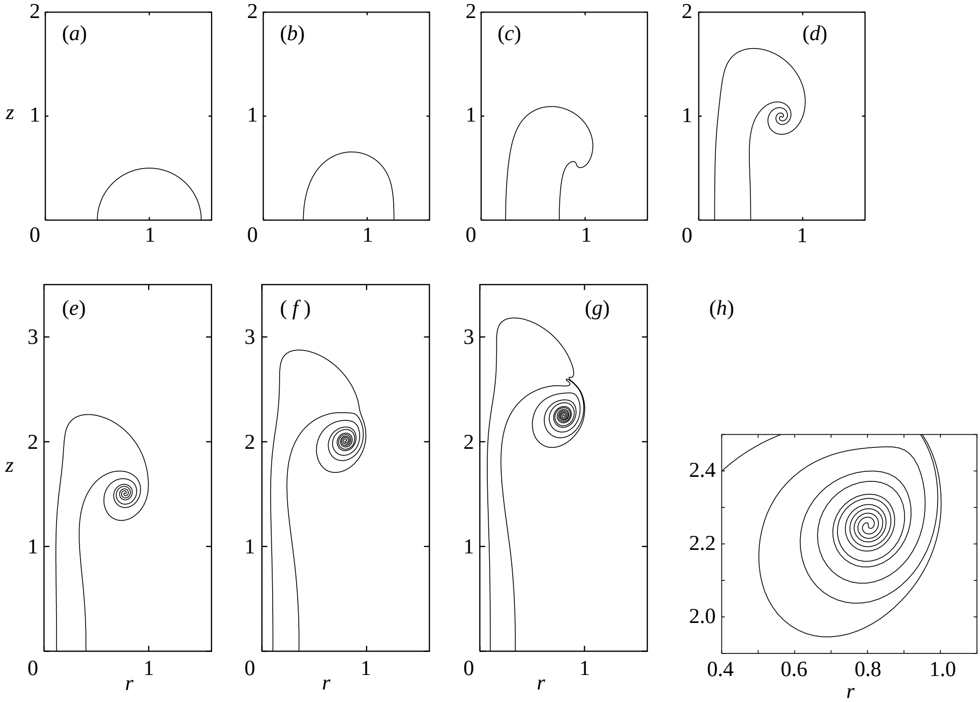

FIGURE 8. Evolution of magnetic torus. Cross-section. Case TC, $r_c = 0.5$. (*a*) $t = 0$, (*b*) 1, (*c*) 2, (*d*) 3, (*e*) 4, (*f*) 5, (*g*) 5.5, (*h*) 5.5, magnified view.

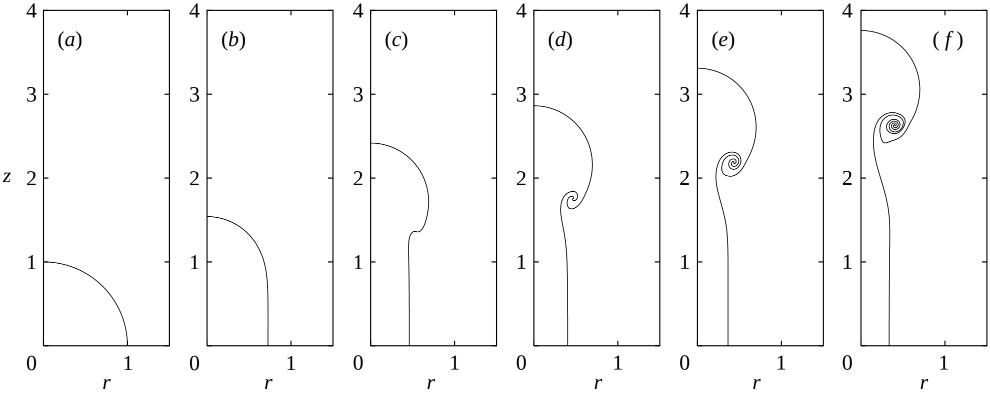

FIGURE 9. Evolution of magnetic sphere. Case SC. Cross-section. (*a*) $t = 0$, (*b*) 2, (*c*) 4, (*d*) 5, (*e*) 6, (*f*) 7.

Roll-up as for the torus case starts at $t \approx 4$, and the number of turns increases with time; compared to the torus case however, the rate of increase is small since the initial curvature of the contour is small.

The contour evolution is compared in figure 10 for the other torus cases. For the circular cores with $r_c = 0.1$ and 0.3 (figure 10*a*, *b*) and the elliptic core elongated in the z-direction (figure 10*d*), the spiral forms so rapidly that the torus is not fully contracted and the formation of spherical fronts is not clear by the end of the simulation. On the other hand, for the circular core with $r_c = 0.8$ (figure 10*c*) and

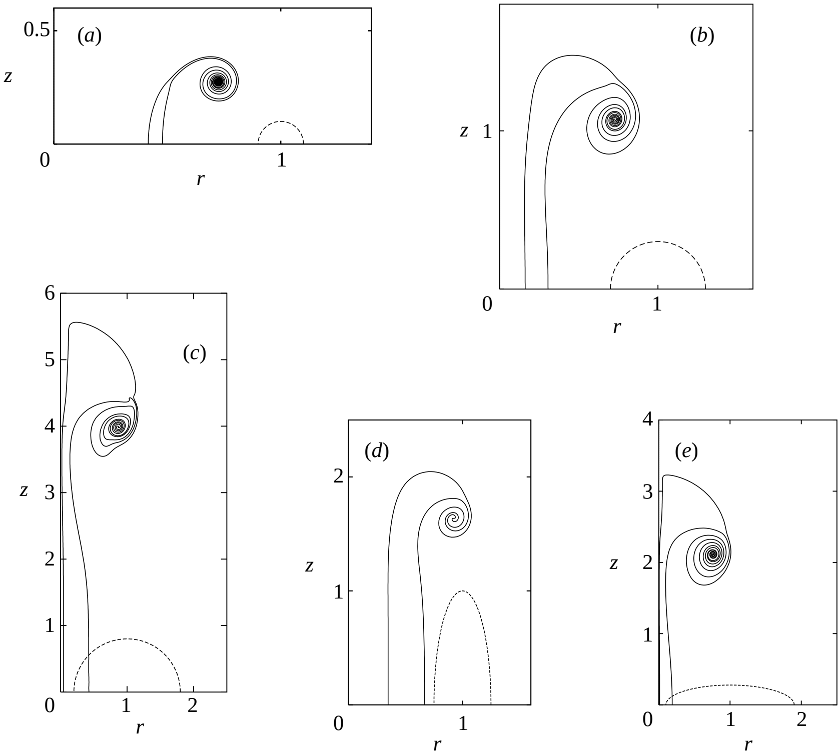

FIGURE 10. Evolution of magnetic torus. Cross-section. The initial shape (dashed line) and a shape near the end of calculation $t = t_1$ (solid line). (*a*) Case TC, $r_c = 0.1, t_1 = 3$, (*b*) Case TC, $r_c = 0.3, t_1 = 4$, (*c*) Case TC, $r_c = 0.8, t_1 = 7$, (*d*) case TE, $a_c = 0.25, t_1 = 4$, (*e*) case TE, $a_c = 0.9, t_1 = 5$.

the elliptic core elongated in the r-direction (figure 10*e*), the eddy contracts until the inside of the hole nearly touches the z-axis and the fronts clearly develop to spherical form.

The evolution of the contours for the other cases of spherical topology are compared in figure 11. Here spherical fronts are seen in both cases. The size of the front is likely to depend on the initial radius of curvature at $r = 0$; the larger radius of curvature leads to the larger front. For the 'cigar' case $(a, b) = (0.5, 2)$, a second roll-up is observed around $(r, z) \approx (0.25, 2.9)$.

5.2.2. *Sheet strength distribution*

Figure 12 shows the evolution of the strength of the vortex sheet Ω for the case of a torus with a circular core of radius $r_c = 0.5$. In this figure $\tilde{l}$ denotes distance along the sheet normalized by its total length; $\tilde{l} = 0$ and 0.5 correspond to the outer and inner point of the intersection with $z = 0$, respectively, while $\tilde{l} = 1$ coincides with $\tilde{l} = 0$. The interval $0.5 \leqslant \tilde{l} \leqslant 1$ covers the upper half of the section ($z \geqslant 0$), the direction of increase of $\tilde{l}$ being clockwise. Note that the same value of $\tilde{l}$ does not generally correspond to the same fluid particle for different instants. At first, the sheet strength becomes large around the top and the bottom where $|\partial R(s, t)/\partial s|$ is large. This leads to a sine-like shape of the sheet strength distribution (figure 12*a*); it is then deformed by the velocity induced by the sheet itself. A sharp peak corresponding to the centre

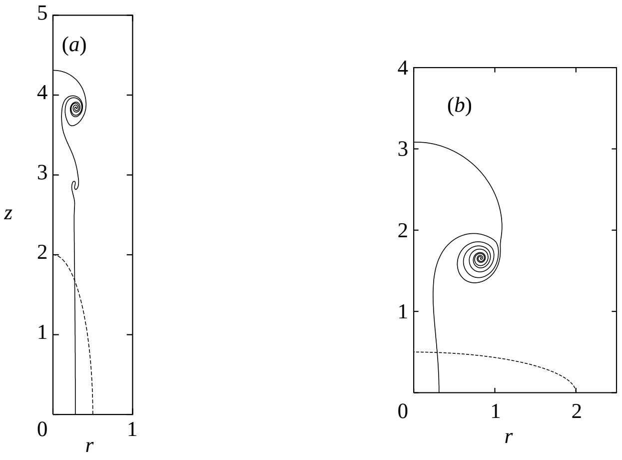

FIGURE 11. Evolution of magnetic sphere. Cross-section. The initial shape (dashed line) and a shape near the end of calculation $t = t_1$ (solid line). (*a*) Case SE, $(a, b) = (0.5, 2)$, $t_1 = 12$, (*b*) case SE, $(a, b) = (2, 0.5)$, $t_1 = 4$.

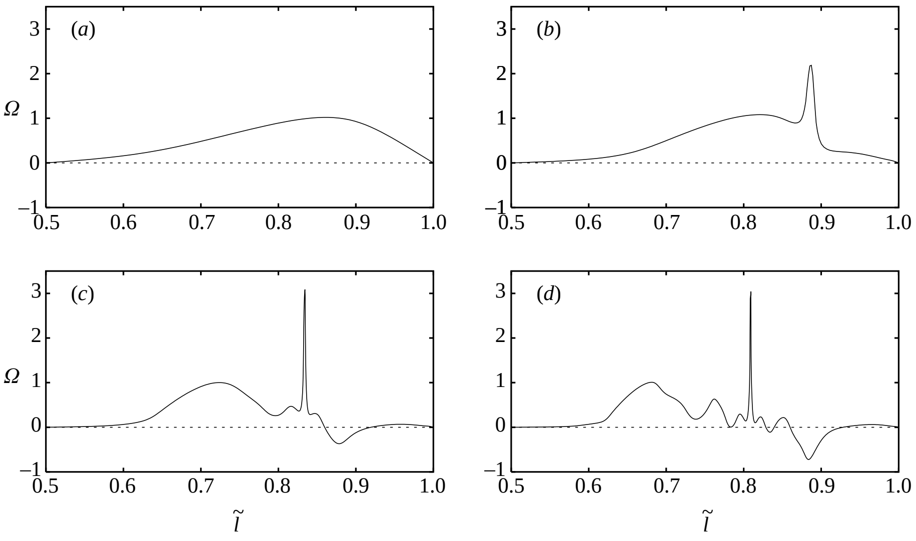

FIGURE 12. Strength of vortex sheet as a function of normalized length for a torus; case TC, $r_c = 0.5$. (*a*) $t = 1$, (*b*) 2, (*c*) 3, (*d*) 4.

of the spiral is observed for $t \gtrsim 2$. As time proceeds, regions of opposite sign of Ω appear: the oscillations seen for $t = 3$ and 4 correspond to the turns of the spiral.

Figure 13 shows the evolution of Ω for the sphere case $(a, b) = (1, 1)$. Here the normalized length $\tilde{l}$ runs from the top of the contour ($\tilde{l} = 0$). The interval $0 \leqslant \tilde{l} \leqslant 0.5$ corresponds to the upper half of the contour. An interval of nearly constant Ω is seen at each instant, this constant being close to unity for $t \gtrsim 2$. This point is discussed with reference to the exact solution (3.2) in § 5.2.4. As in the toroidal case, a sharp peak corresponding to the centre of the spiral is seen for $t = 4, 6$ and the oscillations seen for $t = 6$ correspond roughly to turns of the spiral. Apart from these oscillations, the sheet strength is almost unchanged for $t \gtrsim 2$.

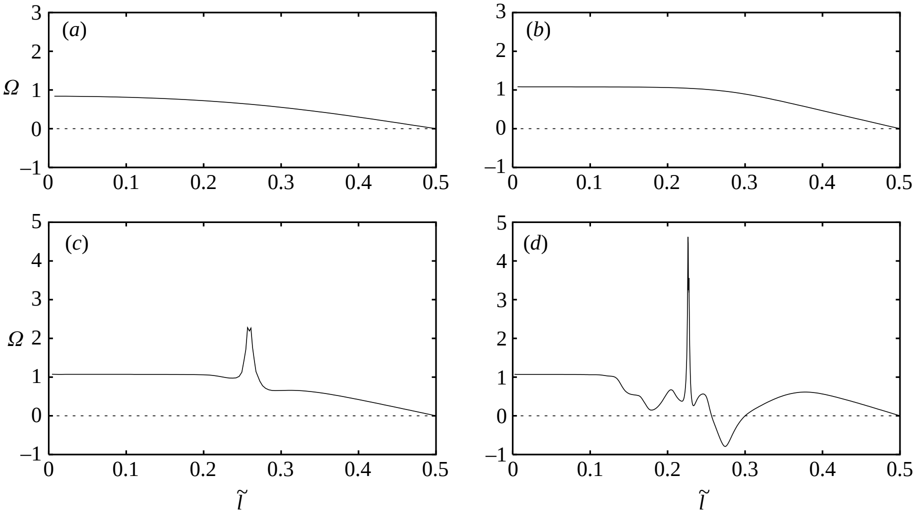

FIGURE 13. Strength of vortex sheet as a function of normalized length for a sphere; case SC. (*a*) $t=1$, (*b*) 2, (*c*) 4, (*d*) 6.

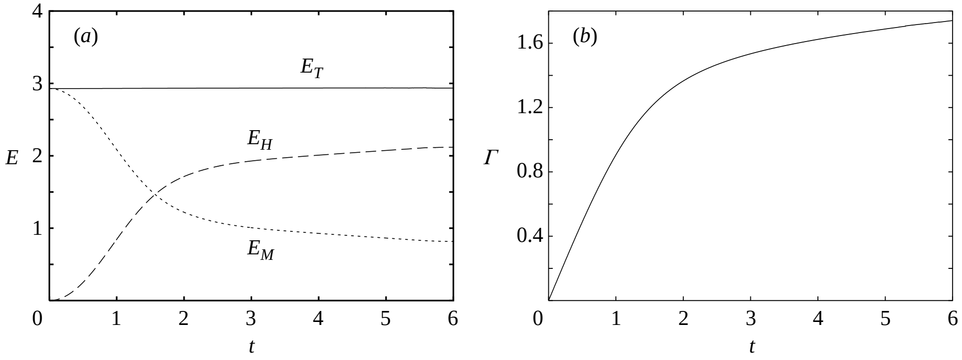

FIGURE 14. Time evolution of (*a*) energy and (*b*) circulation. Case TC, $r_c=0.5$.

5.2.3. *Energy and circulation*

The evolution of energy E and circulation Γ are shown in figure 14 for the case of the torus with a circular core $r_c=0.5$; Γ is the total sheet strength in the upper half, i.e.

$$\Gamma=\int_{z\geqslant 0}\Omega R\,\mathrm{d}l=\int_{z\geqslant 0}\gamma\,\mathrm{d}s.$$

Initially the hydrodynamic energy grows parabolically. The rate of growth, however, becomes small as the eddy approaches the z-axis and the spirals start to form at $t\sim 2$. In consequence, the magnetic energy E_M does not continue to decrease to zero, although there is no topological impediment to such a decrease. The circulation grows linearly for small t. The rate of growth becomes small around $t=2$. It is worth noting that equation (2.23) implies

$$\frac{\mathrm{d}\Gamma}{\mathrm{d}t}=\frac{\kappa^2}{2}\left[R^2(0)-R^2\left(\frac{1}{2}\right)\right],$$

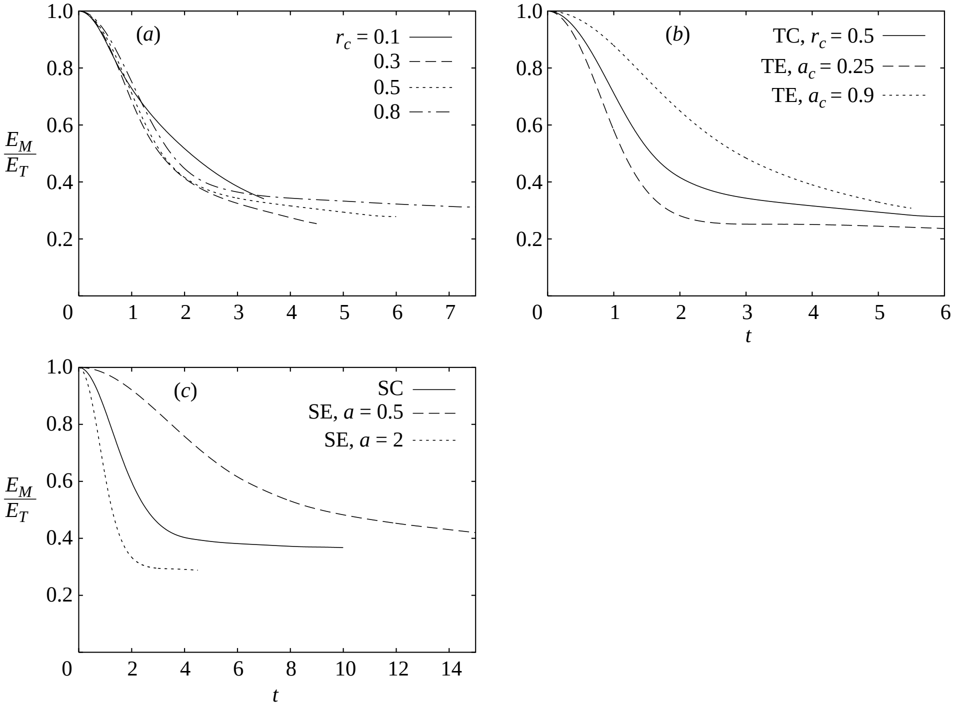

FIGURE 15. Time evolution of magnetic energy fraction. (*a*) Torus case, dependence on core size: cases TC, $r_c = 0.1, 0.3, 0.5, 0.8$; (*b*) torus case, dependence on aspect ratio: case TC, $r_c = 0.5$, cases TE, $a_c = 0.25, 0.9$; (*c*) spherical case.

for torus cases. Thus $|\mathrm{d}\varGamma/\mathrm{d}t|$ becomes small when the torus contracts to the z-axis and becomes thin.

Figure 15 compares the time evolution of the magnetic energy fraction E_M/E_T both for the torus and sphere cases. The lines corresponding to circular core cases collapse for small t (figure 15*a*). This is because the torus moves initially with a constant acceleration which depends on the shape but not on the size of the core. For $r_c = 0.8$, the magnetic energy fraction appears likely to converge to a non-zero value, while this behaviour is not clear for $r_c = 0.1$ and 0.3. For the elliptical cores (figure 15*b*), the lines do not collapse initially since the acceleration depends on cross-sectional shape. For $(a_c, b_c) = (0.9, 0.2778)$, the decay of the magnetic energy fraction is very slow; the value of E_M/E_T is 0.252 at $t = 3$ and 0.236 at $t = 6$. The time evolution for the sphere cases (figure 15*c*) is similar to figure 15(*b*) for elliptic cores with the same direction of elongation.

5.2.4. *Spherical front*

The spherical fronts move almost steadily as seen in figures 8 and 9. A natural question arises: are they related to the exact solution found in §3? The answer is *yes*. Figures 16 and 17 show the radius of curvature and the strength of the vortex sheet near the end of the simulation; $\tilde{l}$ is shifted to adjust the position of the front for torus cases (figure 16). In each case, there is an interval of $\tilde{l}$ in which both R_* and $\varOmega$ are nearly constant. Moreover, the value of $\varOmega$ is close to unity in accordance with the present non-dimensionalization. The speed of the front is obtained by simulation and is compared with the analytical value (3.4), which is $2R_*/3$ in the present case (table 3). The simulation values are calculated using the maximum value of z; for the

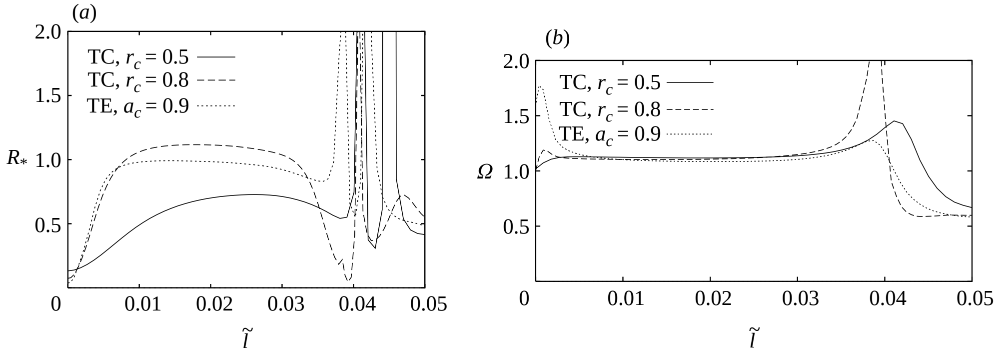

FIGURE 16. Spherical front. Distributions of (*a*) curvature radius and (*b*) strength of the sheet. Torus case. $\tilde{l}$-axis is shifted to adjust the position of the head.

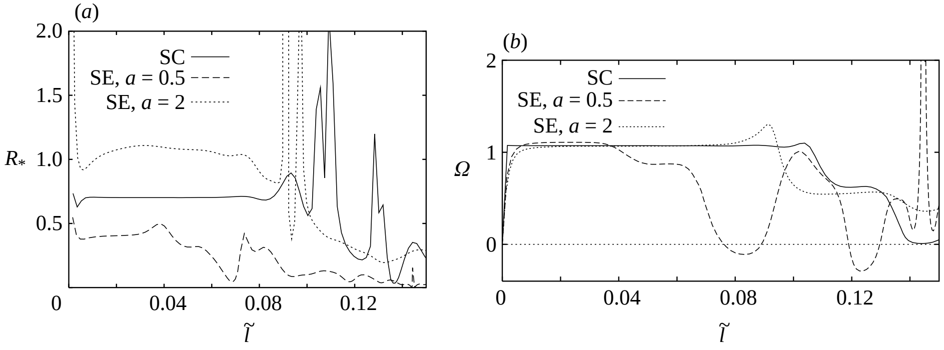

FIGURE 17. Spherical head. Distributions of (*a*) curvature radius and (*b*) strength of the sheet. Sphere case.

Case	Simulation	Analytical
TC, $r_c = 0.5$	0.613	0.468
TC, $r_c = 0.8$	0.757	0.737
TE, $a_c = 0.9$	0.638	0.654
SC	0.450	0.468
SE, $a = 0.5$	0.256	0.266
SE, $a = 2$	0.713	0.722

TABLE 3. Speed of spherical front.

analytical values, the averaged value of R_* in an interval of nearly constant R_* and Ω is used. We see reasonable agreement except for the torus case with a circular core $r_c = 0.5$, for which the spherical fronts are not so clearly formed.

Conservation of energy and volume provides further useful information concerning the relationship between the initial state and the asymptotic state of development. Thus, if the initial magnetic blob is a spheroid of volume V and principal semi-axes a and b, the initial magnetic energy is easily calculated: it is $E_{M0} = \frac{1}{5}\kappa^2 V^{5/3}(3/4\pi)^{2/3}(a/b)^{2/3}$. We have seen that the exact solution for a propagating spherical magnetic vortex of volume V_0 has total energy $E_T = \frac{8}{15}{V_0}^{5/3}\kappa^2(3/4\pi)^{2/3}$. If $V_0 = V/2$ and $E_T = E_{M0}/2$, then all the initial energy can be channelled into the two propagating spherical vortices; this requires that $a/b=8\sqrt{2}/3\sqrt{3}\approx 2.18$. If $a/b>2.18$, then the surplus initial energy is presumably accumulated in the spirals that are observed in the numerical simulations. If $a/b<2.18$, then the volume V_0 of propagating vortices that can be generated is correspondingly reduced.

These results explain the asymptotic behaviour of the magnetic energy described in § 5.2.3: the formation of spherical fronts prevents the magnetic energy from decreasing to zero since the fronts retain a finite fraction of the magnetic energy.

5.3. *Multiple contours: $m \geqslant 1$*

As a step towards dealing with more complex distributions of magnetic field, we now describe some simulations with multiple contours. In principle, any continuous magnetic field B_θ of compact support in the (r, z)-plane can be approximated by a piecewise-constant function (2.27); more precisely, it is possible to take a distribution (2.27) which converges to a given B_θ as $m \to \infty$ in L^2-norm. The use of multiple contours thus provides a route towards treatment of this more general situation.

5.3.1. *Initial magnetic field*

We consider the following continuous distributions of B_θ which have compact supports

$$\frac{B_\theta}{r}=\begin{cases}1-\dfrac{(r-1)^2+z^2}{r_c^2}, & (r-1)^2+z^2\leqslant r_c^2,\\[2ex] 0, & (r-1)^2+z^2>r_c^2,\end{cases}\tag{5.2}$$

for the torus case and

$$\frac{B_\theta}{r}=\begin{cases}1-r^2-z^2, & r^2+z^2\leqslant 1,\\ 0, & r^2+z^2>1,\end{cases}\tag{5.3}$$

for the spherical case. There are various ways to approximate the above distributions by (2.27). For a given m, we choose $\{(\kappa_i, f_i)\}$ $(i=1,2,\ldots,m)$ so that (i) κ_i is the maximum of B_θ/r in the region $\{(r,z)|f_j\geqslant 0,\ j=1,\ldots,i,\ f_j<0,\ j=i+1,\ldots,m\}$ and (ii) $A_i=A_j,\ i,j=1,\ldots,m$; this gives $\kappa_i=(i/m)^{1/2}$ and a natural choice of f_i is $f_i(r,z)=1-\kappa_{i-1}-r^2-z^2$ for the spherical case (figure 18); a similar distribution for the core is used for the torus case. Note that the total energy (i.e. the initial magnetic energy) depends on m, and this should be taken into account in considering the dependence of the results on m.

5.3.2. *Evolution of contours*

Figure 19 shows the evolution of contours for the torus case with $m=4$. The global motion is not very different from the single-contour case shown in figure 8. The contours contract towards the z-axis and are stretched in the z-direction. Frontal structures are also formed. The roll-up, however, is much slower than that in the single-contour case. This is because the strength of each sheet is small, the jump of B_θ/r being reduced from $A=1$ for $m=1$ to $A_i=1/m$. The contours tend to concentrate around the fronts and near the inner boundary of the torus. At $t=5$, fine-scale structures are observed; these differ from those in the single-contour case, presumably because of interaction between the contours.

Figure 20 shows the evolution of contours for the sphere case with $m=8$. We see contraction and stretching which are slower than in the single-contour case. Roll-up

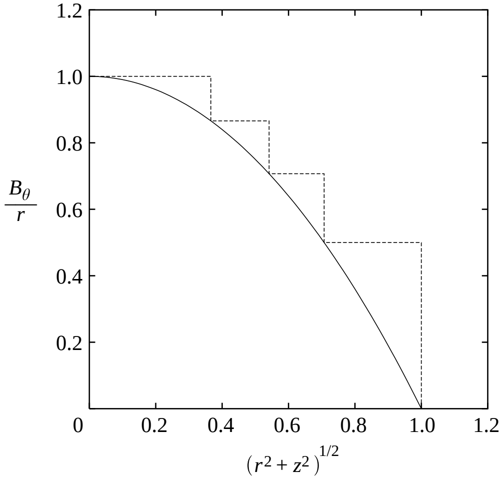

FIGURE 18. Distribution of B_θ/r. Sphere case with $m=4$. Solid line: assumed distribution, dashed line: approximated distribution.

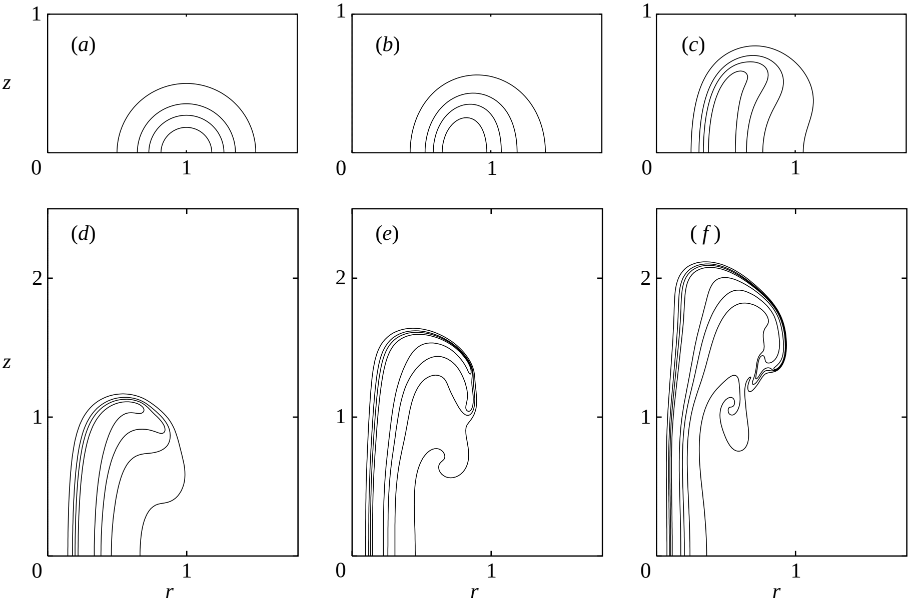

FIGURE 19. Evolution of magnetic torus. $m=4$. Cross-section. (*a*) $t=0$, (*b*) 1, (*c*) 2, (*d*) 3, (*e*) 4, (*f*) 5.

is not observed during the time of simulation. The contours concentrate around the fronts making the effective jump of B_θ/r larger. This jump depends on the position along the surface of the front, in contrast to the single-contour case, although the shapes of the fronts are similar to that in the single-contour case.

5.3.3. *Energy and circulation*

Figure 21 shows the time evolution of magnetic energy fraction. For the torus case (figure 21*a*), its decay rate is initially smaller for larger m because the magnetic force is weaker. At later time, the fraction tends to converge to a value in the range 0.25–0.3.

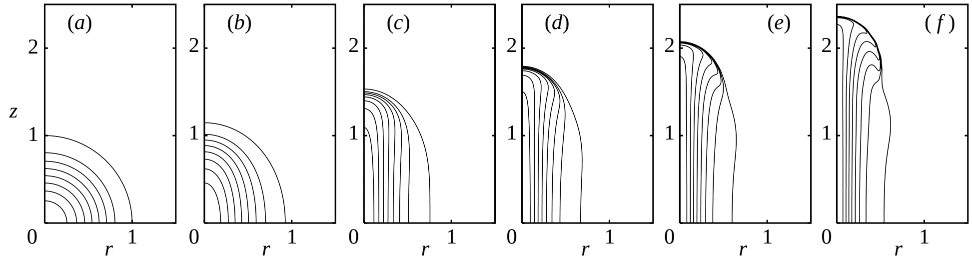

FIGURE 20. Evolution of magnetic sphere. $m = 8$. Cross-section. (*a*) $t = 0$, (*b*) 2, (*c*) 4, (*d*) 5, (*e*) 6, (*f*) 7.

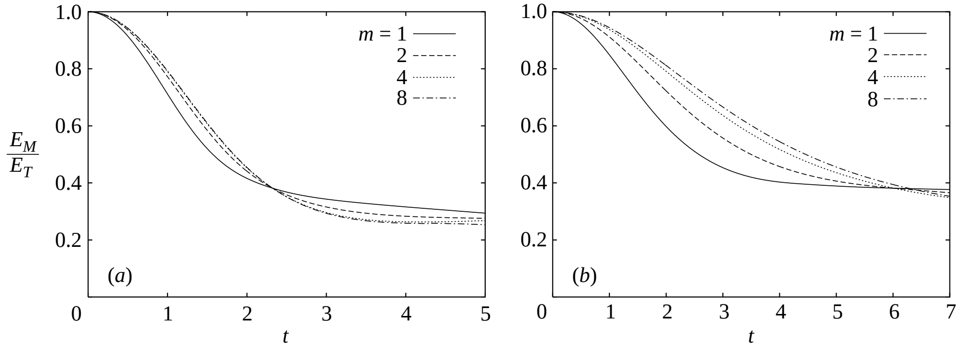

FIGURE 21. Time evolution of magnetic energy fraction. Multiple contours. (*a*) Torus case, (*b*) sphere case.

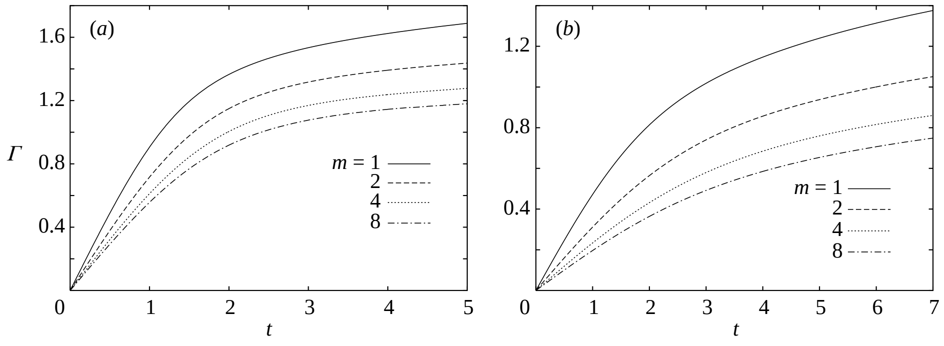

FIGURE 22. Time evolution of total circulation. Multiple contours. (*a*) Torus case, (*b*) sphere case.

The decay rate at $t \approx 5$ is smaller for larger m. For the sphere case (figure 21*b*), the initial evolution is similar to that in the torus case, but the decay rate at $t \approx 7$ is larger for larger m. Of course, this result depends on the particular time chosen, but an instability appears along the front soon after $t = 7$, so that we cannot continue the calculation after this time.

Figure 22 shows the evolution of the total circulation in the upper half of the (r, z)-plane

$$\Gamma = \sum_i \int_{z \geqslant 0} \gamma_i \, \mathrm{d}s_i .$$

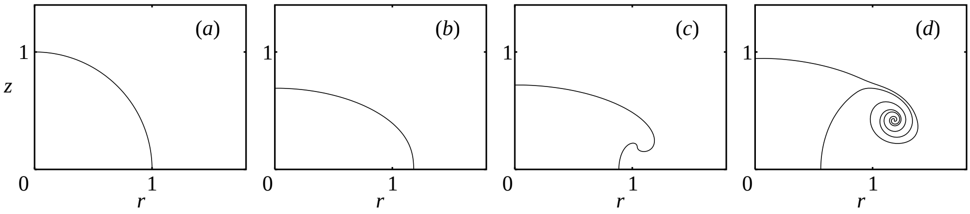

FIGURE 23. Evolution of magnetic sphere under strain. $S=0.3$. Cross-section. (*a*) $t=0$, (*b*) 1, (*c*) 2, (*d*) 4.

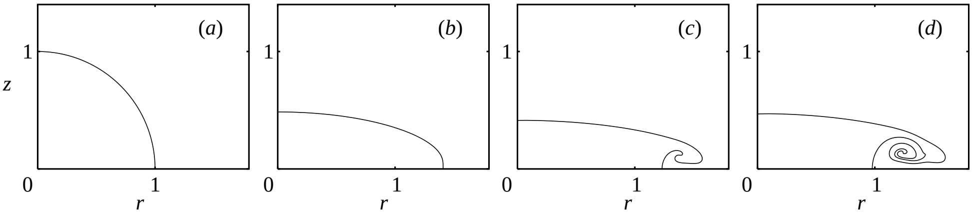

FIGURE 24. Evolution of magnetic sphere under strain. $S=0.5$. Cross-section. (*a*) $t=0$, (*b*) 1, (*c*) 2, (*d*) 3.

As in the single-contour case, we have

$$\frac{\mathrm{d}\Gamma}{\mathrm{d}t}=\sum_i \frac{A_i}{2}\left[R_i^2(0)-R_i^2\left(\frac{1}{2}\right)\right].$$

Since $f_i > f_j$ for $i < j$, the magnitude of $\mathrm{d}\Gamma/\mathrm{d}t$ tends to decrease as m increases. The qualitative features of evolution do not change much with m, however.

6. Evolution under strain

We now consider the effect of incorporating a uniform axisymmetric compressive strain $\boldsymbol{u}_s=(Sr,0,-2Sz)$ on the above analysis. As already indicated in the introduction, this situation was first investigated by Moffatt (1963) for a viscous fluid, where some evidence for the existence of steady disk-shaped magnetic eddies was given. Here, we again restrict attention to the inviscid case. The numerical procedure is the same but with the above strain flow incorporated in (2.24). The strain rate S is set to $0.1, 0.3, 0.5$.

6.1. *Evolution of the contour*

The evolution of the contour for $S=0.1$ is not very different from the case without strain except that initially the contour is passively advected by the strain field. Figures 23 and 24 show the time evolution of the contour for $S=0.3$ and 0.5, respectively. For both cases the contour is initially flattened to form a disk (figures 23*b*, 24*b*), and then roll-up starts around $t=2$. For $S=0.3$ the spirals are advected away from the z-axis by the strain, while for $S=0.5$ they roll up inside the disk. The evolution for $S=0.5$ suggests an approach to a disk-type equilibrium as envisaged by Moffatt (1963): the thickness of the disk reaches a local minimum around $t=2$ and increases gradually for $t>2$ as shown in figure 25(*c*).

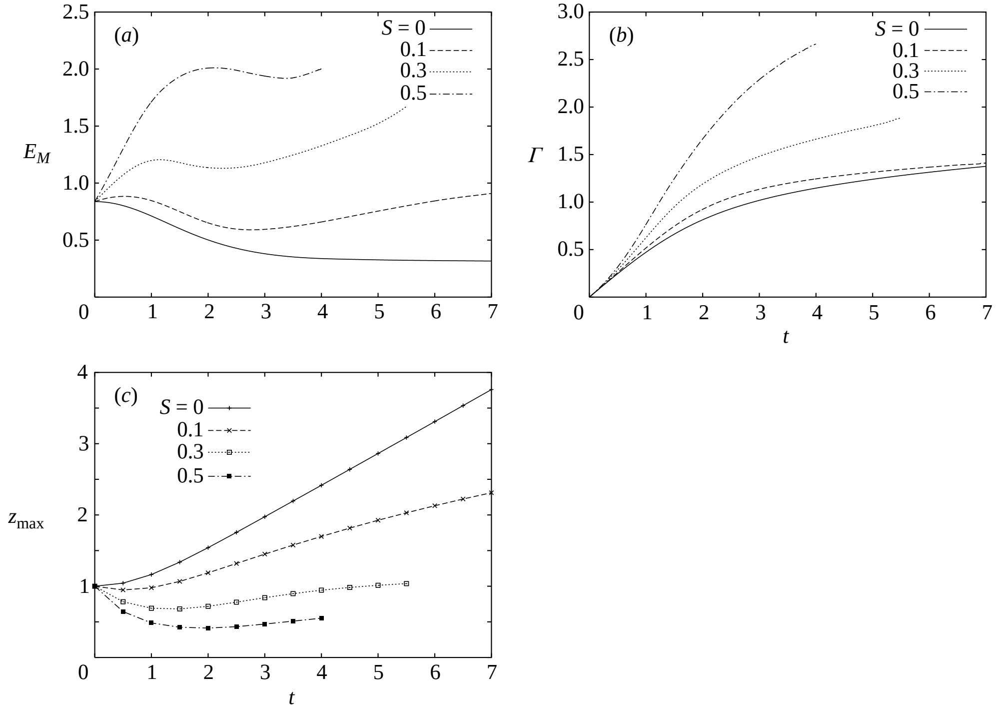

FIGURE 25. Time evolutions of (*a*) magnetic energy, (*b*) circulation and (*c*) $z_{\max}$. Dependence on the strain rate S.

6.2. *Energy and circulation*

Figure 25 shows the evolutions of magnetic energy, circulation and $z_{\max}$, which is a half the disk thickness. (The hydrodynamic energy, including that of the strain field, is infinite and so is not shown.) The case without strain ($S = 0$) is included for comparison. For $S > 0$, the magnetic energy increases initially due to passive advection by the strain field; it then decreases as the Lorentz force causes contraction, and roll-up starts; finally, it increases again, but more slowly than before (figure 25*a*). This behaviour of magnetic energy again suggests the existence of a disk-type equilibrium as a result of a balance between the effects of strain and of the Lorentz force. As S increases, $|\Gamma|$ increases since the strain deforms the eddy so that stronger magnetic forces act upon it (figure 25*b*). The circulation evolves similarly for $S = 0$ and $S = 0.1$. For $S = 0.5$, however, the circulation continues to grow throughout the time of simulation since for sphere cases we have

$$\frac{\mathrm{d}\Gamma}{\mathrm{d}t} = \frac{\kappa^2}{2} R^2\left(\frac{1}{2}\right),$$

where $R(1/2)$ is the value of r where $z = 0$ on the contour. The rate of increase in the thickness of the disk after it attains a local minimum is smaller for larger values of S (figure 25*c*).

7. Concluding remarks

We have developed a contour-dynamics formulation for axisymmetric MHD with purely toroidal magnetic field. A class of exact steady solutions of the ideal MHD equations, which includes Hill's spherical vortex as a special limiting case, has been found. The evolution of toroidal magnetic eddies has been studied numerically using the contour-dynamics formulation. The magnetic energy initially decreases, but this decrease is arrested due to the formation of outward-propagating spherical fronts, which are reasonably well represented by the exact solutions; this result is noteworthy because there is, for the field configuration studied here, no topological barrier to decrease of the magnetic energy to zero. We have also carried out numerical calculation with multiple contours, showing that the method can in principle simulate a magnetic eddy with a general distribution of a magnetic field of compact support. Some numerical evidence is presented suggesting the existence of steady magnetic eddies under the additional effect of imposed compressive strain.

As regards the fate of the magnetic energy, one should note that what happens for extremely high-Reynolds-number flows can be different from the present results for ideal flows. Slow viscous dissipation of energy would then cause a correspondingly slow decay of the 'exact' steady structures described in § 3. For three-dimensional turbulent flows, dissipation is expected to converge to a finite value as the Reynolds number and magnetic Reynolds number tend to infinity. However, even in this much more complex situation, the formation of spherical fronts (a magnetic analogue of 'coherent structures') may be expected to delay the decay of magnetic energy.

The present method is valuable in computational fluid dynamics since it is based on ideal dynamics. Numerical methods in fluid dynamics often require dissipation, sometimes introduced artificially, to ensure stability. Accordingly, most such methods cannot be used for extremely high-Reynolds-number flows. In such situations, Lagrangian methods such as the vortex method or contour dynamics, based as they are on ideal fluid dynamics, provide powerful tools. Although the present paper has been limited to axisymmetric situations for which the velocity is poloidal and the magnetic field toroidal, it provides a starting point for constructing a method for more general MHD flows.

We have shown numerically that the exact solution is subject to the same type of instability as found by Moffatt & Moore (1978) for Hill's spherical vortex: perturbations are swept to the neighbourhood of the rear stagnation point, where a spike grows. One may also anticipate a Kelvin–Helmholtz type of instability, since the surface of the sphere is now a vortex sheet, but this instability is also influenced by the sweeping effect. It is hoped that analytical work in progress will reveal how these two mechanisms of instability interact. It would also be of interest to see how the front of the propagating vortex is affected by three-dimensional disturbances which are absent in axisymmetric simulations.

The deformation of the cross-sections as they evolve, as seen, for example, in figure 8, is similar to that seen in direct numerical simulations of buoyant magnetic flux tubes (Fan, Zweibel & Lantz 1998; Dorch & Nordlund 1998). The main driving force is magnetic tension in our case, whereas it is buoyancy in these simulations. However, as mentioned in § 2.4, buoyancy-driven motion like that induced by Rayleigh–Taylor instability is closely related with the problems considered in this paper, so the similarities are not surprising. Since our formulation assumes vanishing diffusivities, it is perhaps better adapted (than DNS) for very high-Reynolds-number situations.

Finally, possible extension of the contour-dynamics formulation may be anticipated. The present method needs improvement to be applied to more practical problems. One of its limitations is associated with the roll-up of contours, as seen for example in figure 8. Contour surgery as developed by Dritschel (1989) could be used to surmount this difficulty. However, it is not easy here to reconnect contours without creating jumps in the strength of the vortex sheet since this strength depends on both position and time.

Extension to cases with non-vanishing magnetic helicity would also be of interest. However, it would be more difficult to deal with magnetic fields which have both toroidal and poloidal components. For the axisymmetric situation, it may be possible to deal with the case where both the velocity and magnetic fields are purely poloidal by a similar method since the induction equation then reduces to

$$\frac{\mathrm{D}(rA_\theta)}{\mathrm{D}t} = 0,$$

where A_θ is the azimuthal component of the vector potential $\boldsymbol{A}$ of the magnetic field, while the poloidal components of $\boldsymbol{A}$ vanish. Of course, there are problems that need to be overcome, notably that associated with the Lorentz force in the momentum equation: if we simply consider contours of rA_θ so that this quantity has jumps across the contours, then the Lorentz-force term has higher-order singularities which cannot be easily handled. The magnetic helicity vanishes also for this case. However, if this case can be simulated, one can also simulate a toroidal magnetic eddy surrounded by a poloidal magnetic annulus, for which the magnetic helicity does not in general vanish. The case of a toroidal flux tube contracting towards an axial flux tube aligned on the axis of symmetry would be a special case, worth considering.

Y. H. is supported by an overseas research program of MEXT, Japan and is grateful to the kind hospitality of DAMTP, University of Cambridge during his visit. H.K.M. gratefully acknowledges the support of the Chaire Internationale de Recherche Blaise Pascal (2001/3), and of a Leverhulme Emeritus Professorship (2004/5).

REFERENCES

Arnold, V. I. 1974 The asymptotic Hopf invariant and its application. In *Proc. Summer School in Differential Equations, Erevan.* Armenian SSR Acad. Sci. (in Russian) (English transl. *Sel. Math. Sov.* **5**, 327–345, 1986).

Baker, G. R., Meiron, D. I. & Orszag, S. A. 1980 Vortex simulations of the Rayleigh-Taylor instability. *Phys. Fluids* **23**, 1485–1490.

Baker, G. R., Meiron, D. I. & Orszag, S. A. 1982 Generalized vortex methods for free-surface flow problems. *J. Fluid Mech.* **123**, 477–501.

Caflisch, R. E., Li, X. & Shelley, M. J. 1993 The collapse of an axi-symmetric, swirling vortex sheet. *Nonlinearity* **6**, 843–867.

Dorch, S. B. F. & Nordlund, A. 1988 Numerical 3D simulations of buoyant magnetic flux tubes. *Astron. Astrophys.* **338**, 329–339.

Dritschel, D. G. 1989 Contour dynamics and contour surgery: numerical algorithms for extended high-resolution modelling of vortex dynamics in two-dimensional, inviscid, incompressible flows. *Comput. Phys. Rep.* **10**, 77–146.

Fan, Y., Zweibel, E. G. & Norolund, A. 1988 Two-dimensional simulations of buoyantly rising, interacting magnetic flux tubes. *Astrophys. J.* **493**, 480–493.

Ferriz-Mas, A. & Schüssler, M. 1993 Instabilities of magnetic flux tubes in a stellar convection zone I. equatorial flux rings in differentially rotating stars. *Geophys. Astrophys. Fluid Dyn.* **72**, 209–247.

Krasny, R. 1986 A study of singularity formation in a vortex sheet by the point-vortex approximation. *J. Fluid Mech.* **167**, 65–93.

Krasny, R. 1987 Computation of vortex sheet roll-up in the Trefftz plane. *J. Fluid Mech.* **184**, 123–155.

Moffatt, H. K. 1963 Magnetic eddies in an incompressible viscous fluid of high electrical conductivity. *J. Fluid Mech.* **17**, 225–239.

Moffatt, H. K. 1969 The degree of knottedness of tangled vortex lines. *J. Fluid Mech.* **106**, 117–129.

Moffatt, H. K. 1985 Magnetostatic equilibria and analogous Euler flows with arbitrary complex topology Part 1. Fundamentals. *J. Fluid Mech.* **159**, 359–378.

Moffatt, H. K. & Moore, D. W. 1978 The response of Hill's spherical vortex to a small axisymmetric disturbance. *J. Fluid Mech.* **87**, 749–760.

Moore, D. W. 1979 The spontaneous appearance of a singularity in the shape of an evolving vortex sheet. *Proc. R. Soc. Lond.* A **365**, 105–119.

Nitsche, M., Taylor, A. M. & Krasny, R. 2003 Comparison of regularizations of vortex sheet motion. In *Computational Fluid and Solid Mechanics 2003* (ed. K. J. Bathe). Elsevier.

Pozrikidis, C. 1986 The nonlinear instability of Hill's vortex. *J. Fluid Mech.* **168**, 337–367.

Sakajo, T. 2002 Formation of curvature singularity along vortex line in an axisymmetric, swirling vortex sheet. *Phys. Fluids* **14**, 2886–2897.

Schekochinin, A., Cowley, C., Maron, J. & Malyshkin L. 2001 Structure of small-scale magnetic fields in the kinematic dynamo theory. *Phys. Rev.* E **65**, 016305.

Spruit, H. C. 1981 Equations for thin flux tubes in ideal MHD. *Astron. Astrophys.* **102**, 129–133.

Tryggvason, G., Dahm, W. J. A. & Sbeih K. 1991 Fine structure of vortex sheet roll-up by viscous and inviscid simulation. *Trans. ASME*: *J. Fluids Engng* **113**, 31–36.